J Nanopart Res (2018) 20: 319
https://doi.org/10.1007/s11051-018-4412-2

RESEARCH PAPER

Multi-mode photocatalytic performances of CdS QDs modified $CdIn_2S_4/CdWO_4$ nanocomposites with high electron transfer ability

Yannan Liu · Li Li · Run Wang · Jieyun Li · Jiwei Huang · Wenzhi Zhang

Received: 21 June 2018 / Accepted: 31 October 2018 / Published online: 29 November 2018

Abstract In general, quantum dots have the property of generating a plurality of charge carriers using hot electrons or using a single high-energy photon to improve the photocatalytic properties of the material. In this paper, CdS QDs@$CdIn_2S_4/CdWO_4$ modified by CdS QDs was synthesized by the microwave-assisted hydrothermal method, and its composition, crystal structure, morphology, and surface physicochemical properties were well characterized. Electron microscopy results showed that CdS QDs@$CdIn_2S_4/CdWO_4$ composite material exhibited a sheet structure with a length of ca. 350 nm and a width of ca. 50 nm, and CdS QDs uniformly distributes with a diameter of about 5 nm on the sheet structure. UV-visible diffuse reflectance tests showed that the combination of CdS QDs and $CdIn_2S_4$ can extend the light absorption range of $CdWO_4$ to the visible region. Photoluminescence spectroscopy confirmed that CdS QDs had efficient electron transport capabilities. The multi-mode photocatalytic activity of CdS QDs@$CdIn_2S_4/CdWO_4$ showed an excellent ability to degrade organic pollutants. Under the conditions of no co-catalyst and Na_2S-Na_2SO_3 as the sacrificial agent, the hydrogen production of CdS QDs@$CdIn_2S_4/CdWO_4$ can reach 221.3 μmol g^{-1} when exposed to visible light ($\lambda > 420$ nm) for 8 h.

Keywords Microwave-assisted hydrothermal method · CdS QDs · $CdIn_2S_4$ · $CdWO_4$ · Multimode photocatalysis · H_2 evolution · Quantum dots

Introduction

Recently, the sustainable development of photocatalytic technology has motivated more and more scientists to pay attention to the photocatalytic degradation of organic pollutants and photocatalytic hydrogen production from water (Reddy et al. 2014). Among the relevant research studies, semiconductor-based photocatalysis is recognized as one of the ideal technology, which has great potential in solving environmental crisis and energy shortage. Therefore, from the perspective of human development, researchers are committed to developing efficient and stable new semiconductor photocatalysts to degrade organic pollutants and produce clean energy.

In the past decades, many semiconductor photocatalysts have been widely applied in the photocatalysis field, such as metal oxides (TiO_2, ZnO, Cu_2O, etc.) (Hussain et al. 2017; Rokhsat and Akhavan 2016; Mao et al. 2016), metal sulfides (CdS, ZnS, MoS_2, etc.) (Cheng et al. 2017; Zang et al. 2017; Shi et al. 2016), oxyhalides (BiOX, AgX: X = Cl, Br, I) (Xia

Electronic supplementary material The online version of this article (https://doi.org/10.1007/s11051-018-4412-2) contains supplementary material, which is available to authorized users.

Y. Liu · L. Li (✉)
College of Materials Science and Engineering, Qiqihar University, Qiqihar 161006, China
e-mail: qqhrll@163.com; qqhrlili@126.com

Y. Liu · L. Li · R. Wang · J. Li · J. Huang · W. Zhang (✉)
College of Chemistry and Chemical Engineering, Qiqihar University, Qiqihar 161006, China
e-mail: 406301800@qq.com

et al. 2016; Bi et al. 2011), and organic semiconductor materials (g-C_3N_4, PPy, PANI, etc.) (Wang et al. 2009; Pan et al. 2016; Wang et al. 2016a). Relevant studies have shown that some photocatalytic materials do not have a very good range of visible light response, their specific surface areas are in general, and their photogenerated carriers are easily reconfigured. Among these developed photocatalysts, the layered monoclinic cadmium tungstate ($CdWO_4$) is considered to be a potential photocatalytic material due to its excellent chemical structure and good thermal stability. The researchers find that $CdWO_4$ has certain photodegradation and photohydrogen evolution capabilities (Ye et al. 2008). However, as a wide band gap semiconductor, the catalytic performance of $CdWO_4$ is not very satisfactory.

In order to further improve its ability of photocatalytic hydrogen production from water and degrade organic pollutants, $CdWO_4$ can be compounded with other semiconductors to construct a multi-channel electron transfer composite material with energy level matching. Aslam I et al. used rod cadmium tungstate ($CdWO_4$) compound with sheet tungsten trioxide (WO_3) to prepare WO_3/$CdWO_4$ composite materials, in which the degradation of methylene blue had about seven times than pure $CdWO_4$ (Aslam et al. 2014). Xu et al. synthesized CdS modified $CdWO_4$ nanorods by a one-step method. Under the same conditions, the hydrogen production of synthesized composites increased ca. 3.4 and 34 times compared with CdS and $CdWO_4$, and more importantly, CdS modified $CdWO_4$ nanorods had a stable hydrogen evolution ability without any precious metal deposition (Xu et al. 2015). Despite advances in these studies, it is necessary to further explore the coupling of suitable semiconductors with $CdWO_4$ to form novel composite catalysts and to improve the photocatalytic hydrogen production from water and degrade organic pollutants (Mahadadalkar et al. 2018, Wang et al. 2018, Yu et al. 2018, Qian et al. 2018).

Among them, the semiconductor material $CdIn_2S_4$ becomes an ideal material for improving the visible light response of composites. $CdIn_2S_4$ has a narrow bandgap (2.1 eV), and the conduction band position (− 0.76 eV) is more negative (Mousavikamazani et al. 2016). However, the high recombination rate of photogenerated carriers causes the monomer $CdIn_2S_4$ activity is very low, and the formation of a heterojunction by semiconductor recombination can suppress the recombination of photogenerated carriers. For example, a versatile layered $CdIn_2S_4$/graphene nanoheterostructure is prepared as a photocatalyst for solar hydrogen production (Mahadadalkar et al. 2016).

According to the latest research, CdS QDs have been discovered that quantum dots (QDs) show higher extinction coefficient values in the visible region of the solar spectrum than bulk CdS semiconductors, which can reduce the recombination of electron-hole pairs and enhance charge transfer. Meanwhile, it is worth mentioning that quantum confinement effect can make the QD band gap be changed by adjusting the size of QD, that is the conduction band shifts to a more negative potential and the valence band shifts to a more positive potential (Kandi et al. 2017). Therefore, we let the CdS QDs to compound with other semiconductors and found that the presence of CdS QDs can more easily transfer electrons, thus the charge transfer efficiency of the CdS QDs modified composite material can be effectively enhanced.

Based on these researches, the CdS QDs modified $CdIn_2S_4$/$CdWO_4$ nanocomposites were designed and obtained, which have strong absorption in the visible region and can achieve high utilization of sunlight. In this paper, we compared the characteristics of CdS/$CdWO_4$ and CdS QDs/$CdWO_4$ to prove that CdS QDs had high electron transfer ability. In order to enhance the photocatalytic performance of composites and increase the utilization of visible light, the semiconductor $CdIn_2S_4$ was introduced into the synthesis. The combination of CdS QDs, $CdIn_2S_4$, and $CdWO_4$ formed heterogeneous heterojunctions, through virtue of the embedded potential gradient existing between their nanometer-sized interfaces, the separation and transfer of electron-hole pairs were accelerated, and the photostability of the composites was improved. The realization of high-efficiency photocatalytic reaction depends on the fine design and appropriate structure of photocatalyst (Wang et al. 2016b) in this study, and a series of composite materials CdS/$CdWO_4$, CdS QDs@$CdWO_4$, and CdS QDs@$CdIn_2S_4$/$CdWO_4$ are synthesized. It is expected that the effect of CdS QDs with efficient transfer electrons can prolong the separation lifetime of photogenerated electron-holes by comparing CdS QDs with CdS. Meanwhile, we further studied the photocatalytic activity and cycling stability of CdS QDs@$CdIn_2S_4$/$CdWO_4$ nanocomposites by the degradation of organic pollutants under multi-mode photocatalysis and the photolysis of water to produce hydrogen experiments to explore their application prospects.

Experimental

Materials

Cadmium acetate (≥ 99.5%) was purchased from Tianjin Kemiou Chemical Reagent Factory; Thiourea (≥ 99.0%) was purchased from Tianjin Fuchen Chemical Reagent Factory; sodium tungstate (≥ 99.5%) was purchased from Tianjin Kaitong Chemical Reagent Factory. Indium nitrate (≥ 99.5%) was purchased from Sinopharm Chemical Reagent Co. Ltd. Shanghai, China. Mercaptopropionic acid (≥ 98.0%) was purchased from Shanghai Meyer Chemical Technology Co., Ltd. Methyl orange (MO), anhydrous ethanol, and sodium sulfide were all commercially available, analytically pure, and not further purified. All experimental waters were double distilled water.

Preparation of photocatalyst

Synthesis of CdS/$CdWO_4$

Typically, 2.2 mmol of cadmium acetate dissolved in 11 mL of double distilled water and sonicated for 10 min. x mmol (x = 2,3,4) sodium tungstate and 0.04-mmol thiourea dissolved in 10 mL of double distilled water and sonicated for 10 min. Subsequently, the mixed solution was added dropwise to a cadmium acetate solution. After stirring for 2 h, the precursor was transferred to a 100-mL Teflon-lined autoclave and placed in a microwave reactor, and the temperature was maintained at 160 °C for 1.5 h. Finally, the product was washed and dried. According to the different x mmol (x = 2, 3, 4) sodium tungstate samples, the samples were labeled as CdS/$CdWO_4$ (x = 2, 3, 4). Monomer CdS and $CdWO_4$ were prepared by not adding thiourea and sodium tungstate to above steps.

Synthesis of CdS QDs@$CdIn_2S_4$/$CdWO_4$

Typically, 2 mmol of cadmium tungstate was added to 15 mL of double distilled water and sonicated for 10 min. 0.4 mmol of cadmium acetate, 0.8 mmol of indium nitrate, and 1.6 mmol of thiourea were dissolved in 15 mL of double distilled water and sonicated for 10 min. The above-mixed solution was added dropwise to a cadmium tungstate solution. After mixing evenly, the precursor was transferred to a 100-mL Teflon-lined autoclave and placed in a microwave reactor, and the temperature was maintained at 160 °C for 1.5 h. Finally, the product was washed and dried. Taking a certain amount of CdS QDs precursor solution (0.04 mmol of cadmium acetate dissolved in 10 mL of double distilled water. After sonication for 10 min, 30 μL of mercaptopropionic acid was added and dropwise added 1-mol L^{-1} NaOH. The solution was changed from milky white to colorless and transparent. Then 0.04-mmol thiourea was added and stirred until completely dissolved to synthesize CdS QDs precursor solution). The reaction was microwaved at 100 °C for 60 min. After the reaction was completed, it was dried at 60 °C for 8 h to obtain the final product. The synthesis of CdS QDs@$CdWO_4$ with no indium nitrate and thiourea was carried out in the above steps.

Characterization of photocatalyst

X-ray diffraction (XRD) patterns of the samples were analyzed using an X-ray diffractometer from 20° to 80° with $K\alpha$ radiation ($\lambda = 0.15406$ nm) from Bruker-AXS (D8), Germany. X-ray photoelectron spectroscopy (XPS) spectra were measured using a VG-ADES400 X-ray photoelectron spectrometer (Mg K-ADES source residual gas pressure < 10^{-8} Pa test). The scanning electron microscopy (SEM) analysis of the sample was performed using a Japanese scanning electron microscope S-4700 of Hitachi, and the operating voltage was 5 kV. The EDS analysis of the samples was conducted using Model 550i from IXRF, USA. The specific surface area and pore size of the sample were measured by a Quantachrome NovaWin2 physisorption instrument from Contac USA, and the temperature was determined to be 77 K. The TEM and HR-TEM analyses of the samples were conducted using Hitachi H-7650 from Hitachi, Japan and JEM-2100F from Japan JEOL (accelerating voltage of 200 kV). The UV-Vis diffuse reflectance spectroscopy tests of the sample were performed on a TU-1901 UV-Visible double beam spectrophotometer (integrating sphere) manufactured by Beijing General Analysis Corporation. The photoluminescence (PL) spectrum of the sample was measured by the F-7000 fluorescence spectrophotometer of Hitachi High-Tech Science and Technology, Ltd. Japan.

Photocatalytic experiment

The detailed process of multi-mode photocatalytic degradation experiments can be found in the existing literature reports for our research group (Chen et al. 2016a). In this study, MO was used as the model molecule on the photocatalytic activity of the sample. First, the photocatalyst (0.15 g under ultraviolet light, 0.15 g under simulated sunlight, and 0.3 g under visible light) was dispersed in a solution to MO (50 mg L^{-1}), sonicated for 10 min, and stirred for 30 min in the dark to achieve an adsorption-desorption equilibrium. Excite the light source, and start the photocatalytic experiment after the light source was stable. At certain time intervals, 3 mL of the suspension was collected and centrifuged to remove the catalyst, and the concentration of MO was determined by measuring the absorbance (at $\lambda_{max} = 463$ nm) using an UV-Vis spectrophotometer (model TU-1901). The photocatalysis and measurement processes of other organic pollutants are the same as the degradation of the MO process. After the photocatalyst was washed with ethanol and deionized water, it was dried and recovered for use.

Photocatalytic H_2 evolution from water splitting

The photocatalytic hydrogen production experiment was carried out in a vacuum reactor connected by a closed circulation system (LabSolar-IIIAG photocatalytic online analysis system, Beijing Bofeilai Co., Ltd.). One hundred milligrams of photocatalyst was dispersed in 50 mL of distilled water, and Na_2S-Na_2SO_3 sacrificial agent (0.2-mol Na_2S and 0.3-mol Na_2SO_3) was added. The light source is a 300-W Xe lamp (PLS-SXE300), 10 cm from the reaction solution; high purity nitrogen as a carrier gas, the flow rate is 0.5 mL/s; the output pressure is 0.4~0.5 MPa, and the working voltage and operating current are approximately 20 mV and 50 mA. During the reaction, circulating cool water maintains the temperature of the reactor at about 5 °C. The detector type is TCD and the chromatography uses 5-Å molecular sieves. The photocatalytic activity of the samples was investigated by collecting the amount of H_2 produced 8 h after light irradiation.

Results and discussion

XRD analysis

In order to study the crystal structure of the samples, XRD analysis was performed on the different products including CdS, $CdWO_4$, CdS/$CdWO_4$, CdS QDs/$CdWO_4$, and CdS QDs@$CdIn_2S_4$/$CdWO_4$. Discovered from Fig. 1, diffraction peaks of pure $CdWO_4$ correspond to monoclinic phase (JCPDS card 14-0676) (Xu et al. 2015), and the strong and sharp peaks shown in the figure indicate that the sample has a high degree of crystallinity. The pure CdS belongs to the hexagonal phase structure and corresponds to (100), (002), (101), (110), (103), and (112) crystal planes of the standard JCPDS card 06-0314 (Yan et al. 2017). No other peak appears in the XRD pattern, indicating that the resulting crystal phase has high purity. The XRD results of the composites in Fig. 1a are composed of a monoclinic phase $CdWO_4$ and a hexagonal phase CdS. The 2θ value corresponding to the left-shaded mark peak is 35.37°, which is consistent with the (002) crystal plane in $CdWO_4$ (Xu et al. 2015). The right shadow-labeled peak which corresponds to a 2θ value of 43.68° can be attributed to the (110) crystal plane in CdS (Yan et al. 2017). It can be seen from Fig. 1a that with the change of CdS content, the crystallinity of the composite material changes with the sharpness and intensity of the diffraction peak.

Especially, CdS/$CdWO_4$ (x = 2) can be clearly observed characteristic peaks of CdS. The diffraction peak labeled as ◆ in Fig. 1b corresponds from left to right to the (002) and (− 202) crystal planes in $CdWO_4$, and the diffraction peak labeled as ♥ corresponds to the cubic crystal phase $CdIn_2S_4$ (JCPDS card 27-0060) from left to right is the (311), (400) crystal plane. The above results indicate that both $CdWO_4$ and $CdIn_2S_4$ exist in the composite material. In addition, the same characteristic diffraction peaks as those of monomer $CdWO_4$ exist in CdS QDs@$CdWO_4$ and CdS QDs@$CdIn_2S_4$/$CdWO_4$ in Fig. 1b, indicating that the composite still retains the crystal structure of the original $CdWO_4$, and the phase is no change. At the same time, the strong and sharp diffraction peak of CdS QDs@$CdIn_2S_4$/$CdWO_4$ nanocomposite proves that the composite has good crystallinity. Excellent crystallinity is one of the main influencing factors of composite photocatalytic performance. According to the photocatalytic performance test described below, CdS QDs@$CdIn_2S_4$/$CdWO_4$

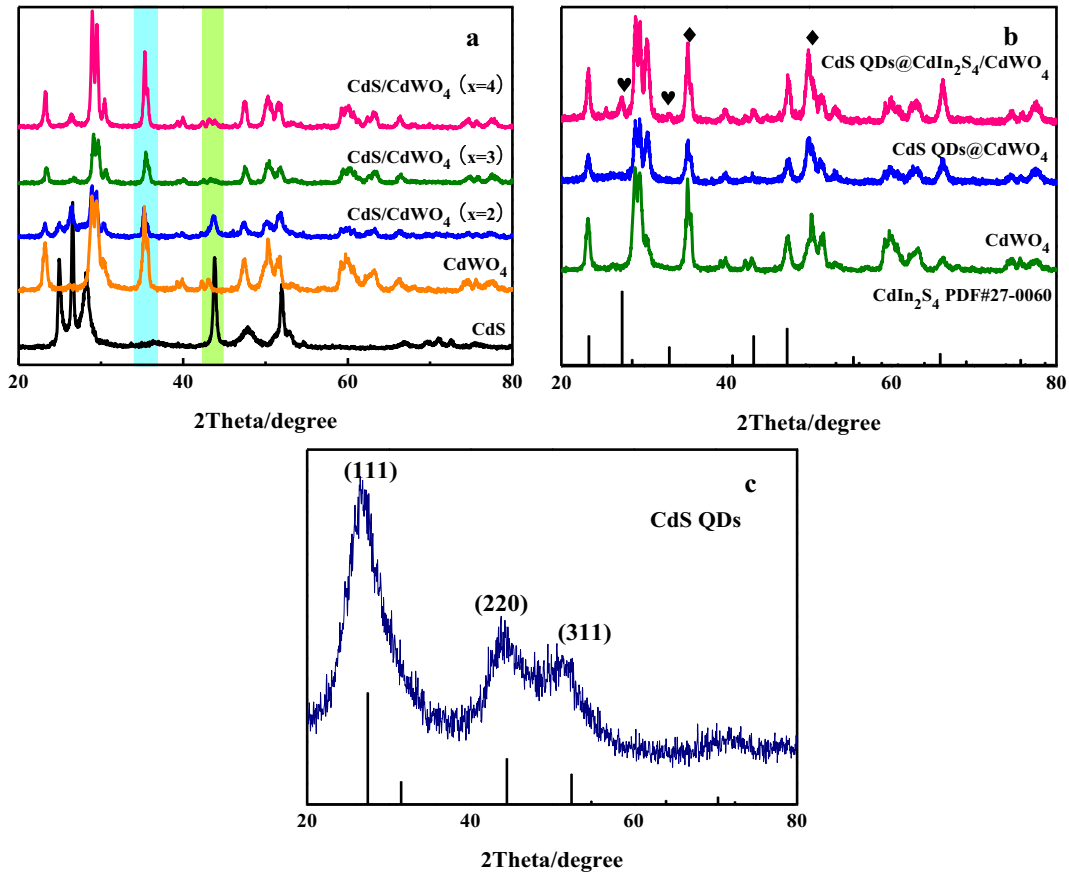

Fig. 1 X-ray diffraction patterns of different samples: **a** CdS, $CdWO_4$, and different ratio CdS/$CdWO_4$; **b** $CdWO_4$, CdS QDs@$CdWO_4$, and CdS QDs@$CdIn_2S_4$/$CdWO_4$; and **c** CdS QDs

nanocomposite exhibits excellent degradation effect on MO. It is worthy that diffraction peaks of CdS QDs could not be observed in the XRD pattern. This result can be attributed to the low content of CdS QDs in the composite material that could not be detected. In order to study the crystalline structure of the CdS QDs synthesized, XRD measurements were performed. The results are shown in Fig. 1c. As can be seen from Fig. 1c, CdS QDs (standard JCPDS card 89-0440) are cubic phases and diffraction peaks of the synthesized samples correspond to the (111), (220), and (311) crystal planes, respectively. It is consistent with CdS QDs reported in the literature (Lei and Jing 2011), proving that the CdS synthesized in this paper is indeed CdS QDs.

The crystallite sizes of $CdWO_4$, CdS QDs@$CdWO_4$, and CdS QDs@$CdIn_2S_4$/$CdWO_4$ were calculated according to Scherrer's formula. The results are shown in Table 1.

In order to calculate the lattice strain of the sample, the average grain size and lattice stress of $CdWO_4$, CdS QDs@$CdWO_4$, and CdS QDs@$CdIn_2S_4$/$CdWO_4$ were calculated using the Williamson and Hall equations. The results are shown in Table 1:

$$B\cos\theta/\lambda = \eta\sin\theta + 1/D$$

Here, B is the width of the X-ray diffraction peak (full width at half maximum), β represents the Bragg diffraction angle, λ represents the X-ray wavelength, and η represents the lattice strain. The $\eta\sin\theta$ is plotted on the X-axis, and the $B\cos\theta/\lambda$ is plotted on the Y-axis. D is the grain size. The sloping lines of $\eta\sin\theta$ and $B\cos\theta/\lambda$ represent the estimated strain of the lattice. The results are shown in Fig. 2. According to this method, the intercept in the figure is the crystallite size, and the obtained value is consistent with the Scherrer's equation. Due to the difference in lattice constants between CdS QDs and $CdIn_2S_4$ and $CdWO_4$, the stress near the growth interface during the nanocomposite composite process will be distorted. At the same time, this lattice mismatch phenomenon results in a shift in the lattice

Table 1 Lattice constants (Å), average grain sizes (nm), bandgap energy (eV), and lattice stress (%) for different synthetic products

Sample	Crystal parameters			Crystallite size(nm)		*Eg*/eV	Lattice strain (%)
	a/Å	*b*/Å	*c*/Å	D_s	D_w		
$CdWO_4$	5.0353	5.8764	5.0787	24.3	25.1	3.70	− 0.73%
CdS QDs@$CdWO_4$	5.0348	5.8458	5.0771	27.3	27.2	2.25	+ 0.55%
CdS QDs@$CdIn_2S_4$/$CdWO_4$	5.0338	5.8305	5.0769	26.7	26.8	2.15	+ 0.62%

Note: D_s: grain size calculated using Scherrer; D_w: grain size calculated using Williamson and Hall method

stress of $CdWO_4$ from a negative value to a positive value, indicating that there is the interaction between composites (Khanchandani et al. 2014).

Surface morphology and microstructure analysis

In order to study the surface morphology of different samples, the samples $CdWO_4$, CdS QDs@$CdWO_4$, and CdS QDs@$CdIn_2S_4$/$CdWO_4$ were analyzed by SEM and HR-TEM. The results are shown in Fig. 3. Figure 3a–c shows micrographs of $CdWO_4$, CdS QDs@$CdWO_4$, and CdS QDs@$CdIn_2S_4$/$CdWO_4$ by TEM at the same magnification. As can be seen from Fig. 3a, the monomer $CdWO_4$ is a staggered rod-like structure. From Fig. 3b, c, it is not difficult to find that the morphology of the sample has not changed significantly with the loading of CdS QDs and $CdIn_2S_4$. In addition, the TEM results of CdS/$CdWO_4$ (x = 2) show that there is no a significant change in the structure of the rod-like sheet $CdWO_4$ (Fig. S1). According to the surface element analysis of EDS (Figs. S2 and S3) for CdS QDs@$CdIn_2S_4$/$CdWO_4$, it can be seen that the elements are evenly distributed on the surface of CdS QDs@$CdIn_2S_4$/$CdWO_4$ catalysts, which indicates that $CdIn_2S_4$ and CdS QDs are uniformly distributed on $CdWO_4$. The thin rod-like structure with uniform distribution of CdS QDs and $CdIn_2S_4$ can make the organic contaminant fully contact with the surface of the composite material. It increases the contact area between the reactant and the nanocomposite material, thereby significantly enhancing the photocatalytic activity. Therefore, according to the following result, CdS QDs@$CdIn_2S_4$/$CdWO_4$ has the best photocatalytic performance.

In order to further observe the morphology of CdS QDs@$CdIn_2S_4$/$CdWO_4$ under microscopic conditions, TEM and HR-TEM analyses were performed. The results are shown in Fig. 3d–e. CdS QDs@$CdIn_2S_4$/$CdWO_4$ exists as thin rods, with a length of ca. 350 nm and a width of ca. 50 nm, and black dot-like particles are distributed on the rod in Fig. 3d. The lattice fringes in the enlarged part of this region are shown in Fig. 3e. The presence of CdS QDs with a diameter of about 5 nm can be clearly observed in lattice staggered interlacing, and lattice fringes can be obtained through inverse fast Fourier transform (IFFT) of different selected regions in Fig. 3f–h and Fourier lines see Fig. S4. Among them, the lattice spacing of the (111) plane corresponding to the cubic CdS QDs is 0.337 nm in Fig. 3g, which is in agreement with the literature (Ge et al. 2012). It is proved that the CdS QDs exist in the

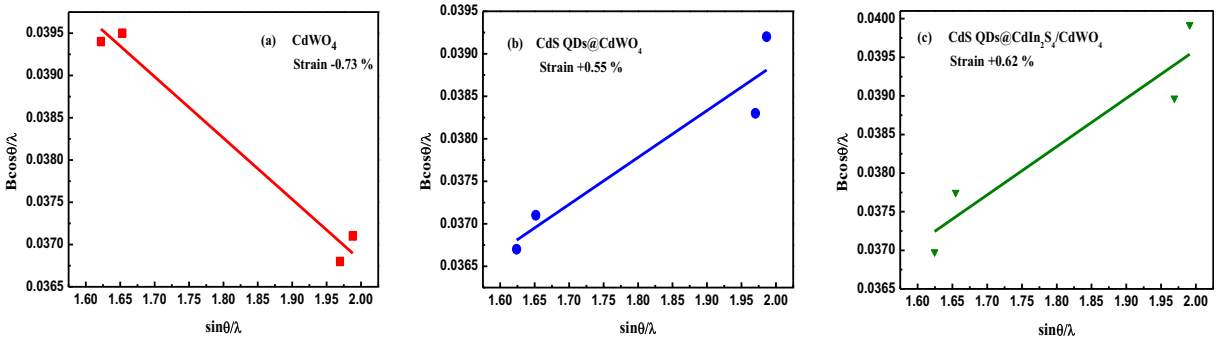

Fig. 2 Williamson-Hall plots for the products of $CdWO_4$, CdS QDs@$CdWO_4$, and CdS QDs@$CdIn_2S_4$/$CdWO_4$

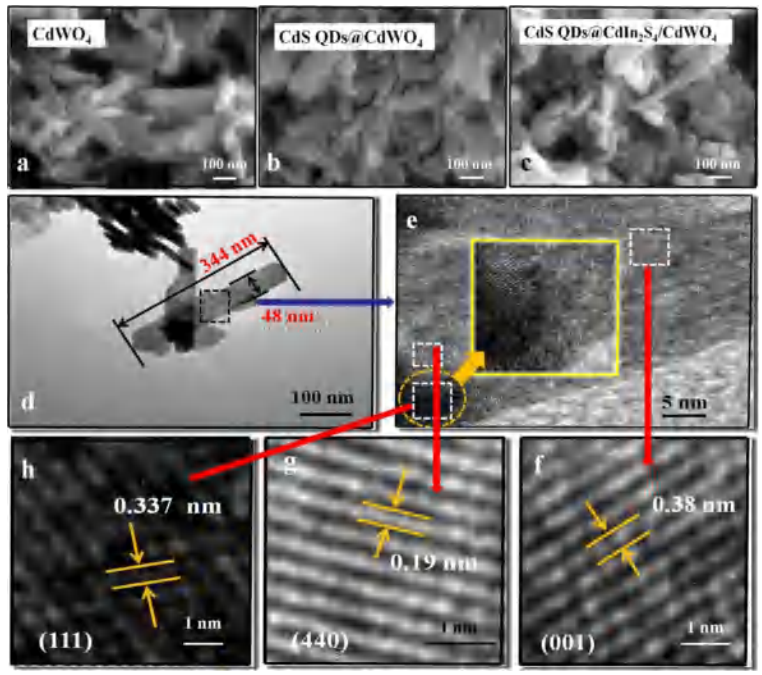

Fig. 3 SEM of $CdWO_4$, CdS QDs@$CdWO_4$, and CdS QDs@$CdIn_2S_4$/$CdWO_4$(**a**–**c**); TEM of CdS QDs@$CdIn_2S_4$/$CdWO_4$ (**d**); H-TEM micrographs of CdS QDs@$CdIn_2S_4$/$CdWO_4$ (**e**); lattice fringe photos of $CdWO_4$, $CdIn_2S_4$, CdS QDs (**f**–**h**)

CdS QDs@$CdIn_2S_4$/$CdWO_4$ nanocomposites. The lattice spacing of 0.38 nm in Fig. 3f corresponds to the (011) crystal plane (Ling et al. 2010) of the monoclinic phase $CdWO_4$, and the lattice spacing of 0.19 nm in Fig. 3g corresponds to the cubic phase of the (440) plane $CdIn_2S_4$ (Chen et al. 2016b). These results consistent with the above XRD analysis, it was further proved that the presence of $CdIn_2S_4$ and $CdWO_4$ in the nanocomposites in this article. As combined with PL analysis, due to the multiple transport pathways of photogenerated carriers, the electron-hole pair recombination rate is reduced, CdS QDs@$CdIn_2S_4$/$CdWO_4$ nanocomposites show the lowest intensity compared to $CdWO_4$, CdS QDs/$CdWO_4$. It is also indicating the formation of heterojunctions of CdS QDs@$CdIn_2S_4$/$CdWO_4$ nanocomposites.

XPS analysis

The surface chemical compositions and the valence state of CdS QDs@$CdIn_2S_4$/$CdWO_4$ are measured by XPS, as shown in Fig. 4. The presence of the C element can be attributed to the instrument, and the other peaks are mainly derived from the five elements containing O, W, Cd, In, and S on the surface of CdS QDs@$CdIn_2S_4$/$CdWO_4$ in Fig. 4a. Figure 4b is an XPS pattern of W 2f, and the binding energies of W $2f_{5/2}$ and W $2f_{7/2}$ are 37.4 and 35.3 eV, respectively, indicating that the presence of the tungsten element on the sample is the W^{6+} chemical state (Zhan et al. 2016). The binding energies of In $3f_{5/2}$ and In $3f_{3/2}$ are 444.6 and 452.2 eV, respectively, indicating that the indium is the In^{2+} chemical state (see Fig. 4c) (Zhang et al. 2013) As Fig. 4d shown, Cd $3d_{5/2}$ and Cd $3d_{3/2}$ which correspond to the binding energies are 404.7, 405.5, 411.4 eV, and 412.3 eV, inferring that the presence of the cadmium element is Cd^{2+} (Chen et al. 2016c; Zhang et al. 2016). The XPS pattern of O 1s at 532.5 eV is attributed to the lattice oxygen (Zheng et al. 2015); the binding energy for the 531.1 eV is attributed to the hydroxyl oxygen in the sample (Liang et al. 2014); the binding energy for the 529.9 eV is attributed to the adsorbed oxygen (see Fig. 4e) (Liu et al. 2015). The S 2p XPS spectra are showed in Fig. 4f. The two centering at 161.1 and 162.3 eV, showing a peak separation of 1.2 eV, can be attributed to the S^{2-} (Zhang et al. 2013).

UV-visible diffuse reflectance and PL photoluminescence spectra analysis

In order to investigate the visible light absorption properties of the composites, UV-Vis diffuse reflectance measurements of the samples $CdWO_4$, CdS, CdS QDs, CdS QDs@$CdWO_4$, CdS/$CdWO_4$, and CdS QDs/$CdIn_2S_4$/

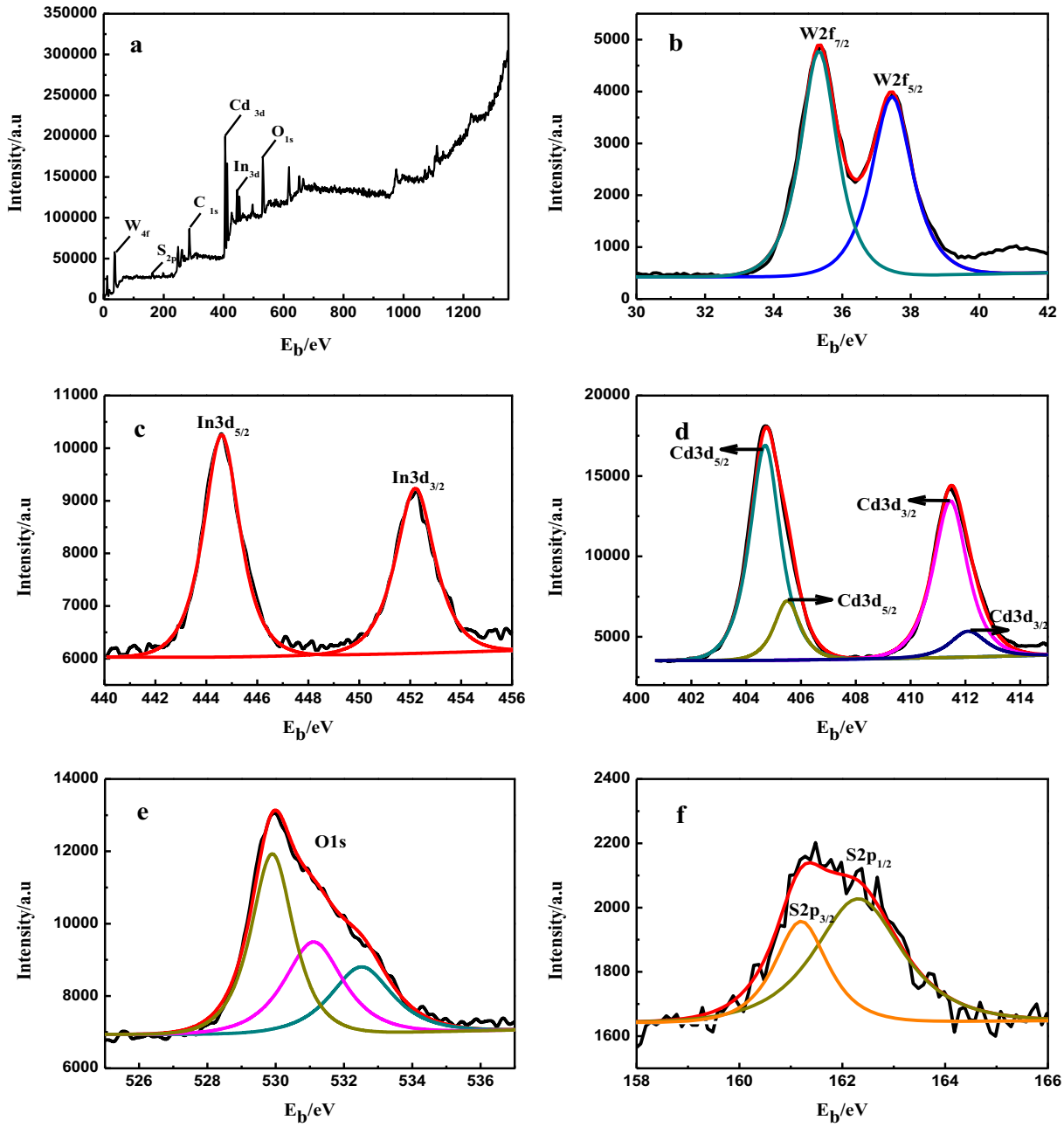

Fig. 4 X-ray photoelectron spectrogram of CdS QDs@$CdIn_2S_4$/$CdWO_4$ nanocomposites (**a** full spectrum, **b** W4f, **c** In3d, **d** Cd3d, **e** O1s, **f** S2p)

$CdWO_4$ were performed and the results are shown in Fig. 5. Figure 5 which shows the wide bandgap semiconductor $CdWO_4$ has a response in the ultraviolet region (Jia et al. 2016) with an absorption band edge of approximately 365 nm. After compounding with the narrow bandgap semiconductor CdS, the light absorption of the composite material broadens into the visible light region. At the same time, both CdS and CdS QDs have strong absorption peaks in the visible region and redshift to visible region of CdS QDs in Fig. 5a. The redshift of absorption bands of CdS QDs@$CdWO_4$, CdS/$CdWO_4$, and CdS QDs@$CdIn_2S_4$/$CdWO_4$ composites increase by 168, 203, and 225 nm, respectively, compared with that of CdWO4, when CdS, CdS QDs, $CdIn_2S_4$, and $CdWO_4$ are compounded. Figure 5d shows that the bandgap of CdS is narrower than that of CdS QDs, which is due to

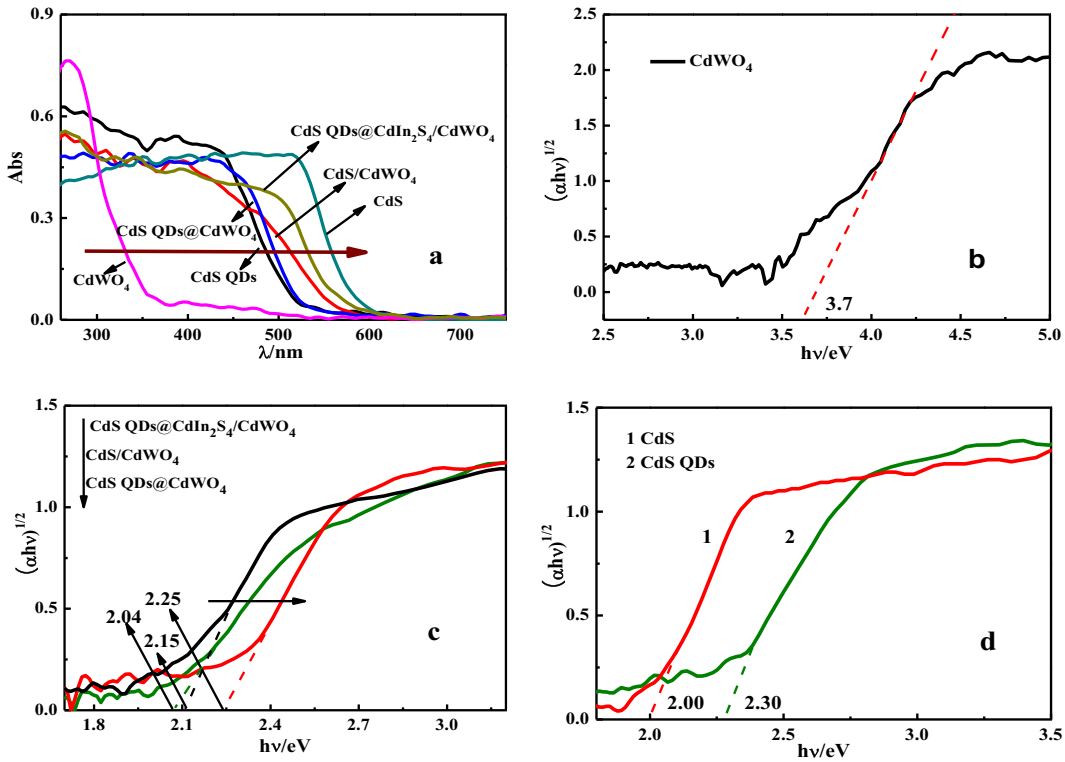

Fig. 5 **a** UV-Vis/DRS absorption spectra of CdS, $CdWO_4$, and CdS QDs@$CdWO_4$, CdS/$CdWO_4$, and CdS QDs@$CdIn_2S_4$/$CdWO_4$ nanocomposites. **b** Kubelka-Munk energy curve plot curve $CdWO_4$. **c** Kubelka-Munk energy curve plot for CdS QDs@$CdWO_4$, CdS/$CdWO_4$, and CdS QDs@$CdIn_2S_4$/$CdWO_4$. **d** CdS and CdS QDs Kubelka-Munk energy curve plots

the quantum size effect of CdS QDs. That is, as the QD size decreases, the bandgap value becomes wider (Ma et al. 2017). The bandgap estimates for different samples were obtained based on the Kubelka-Munk plot curve: $\alpha h\upsilon = A(h\upsilon - Eg)^2$. Among them, α, $h\upsilon$, A, and Eg denote the light absorption coefficient, the photon energy, the proportionality constant, and the bandgap value, respectively. The results are shown in Tables 1 and 2. Seeing Table 2 and Fig. 5, CdS QDs, $CdIn_2S_4$, and $CdWO_4$ have a suitable bandgap. The complex formation of CdS QDs@$CdIn_2S_4$/$CdWO_4$ has better photocatalytic activity because the matched band structure between semiconductors can reduce the unnecessary binding of electrons and holes to the surface of the material and further enhance the separation between the excitation electrons and holes.

Table 2 Electronegativity (eV), energy band gaps (eV), conduction band edge, and valence band edge potential E/(eV) of $CdWO_4$, $CdIn_2S_4$, CdS QDs, and CdS

Semiconductor	X (eV)	Eg (eV)	E_{CB} (eV)	E_{VB} (eV)
$CdWO_4$	6.28	3.7	− 0.07	3.63
$CdIn_2S_4$	4.79	2.1(Carević et al. 2015)	− 0.76	1.34
CdS QDs	5.04	2.30	− 0.61	1.69
CdS	5.04	2.00	− 0.46	1.54

PL is an effective technique for studying the excitation, trapping, and transfer of photo-induced charge carriers. In order to study the separation of electron-hole pairs of $CdWO_4$, CdS QDs@$CdWO_4$, CdS/$CdWO_4$, and CdS QDs@$CdIn_2S_4$/$CdWO_4$, PL analysis was performed as shown in Fig. 6. The $CdWO_4$ photocatalyst has a strong emission peak around 458.4 nm at room temperature (Xu et al. 2015; Ling et al. 2010). The luminescence intensity of CdS QDs@$CdWO_4$, CdS/$CdWO_4$, and CdS QDs@$CdIn_2S_4$/$CdWO_4$ composites is lower than $CdWO_4$. In addition, in order to further demonstrate the high-efficiency electron transfer ability of CdS QDs, the PL spectra of CdS/$CdWO_4$ and CdS QDs@$CdWO_4$ were analyzed. The results showed that the luminescence intensity of CdS QDs@$CdWO_4$ was

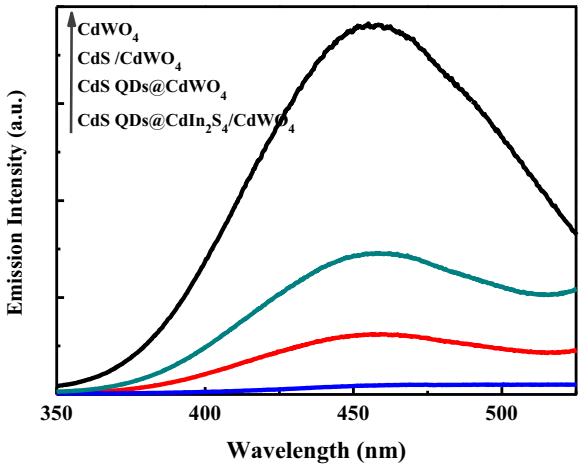

Fig. 6 Photoluminescence spectra of $CdWO_4$, CdS/$CdWO_4$, CdS QDs@$CdWO_4$, and CdS QDs@$CdIn_2S_4$/$CdWO_4$ ($\lambda_{ex} = 280$ nm)

significantly reduced, indicating that compared with CdS, CdS QDs had high electron transfer ability due to their quantum locality and small size. At the same time, it is evident from Fig. 6 that the luminous intensity of CdS QDs@$CdIn_2S_4$/$CdWO_4$ nanocomposites is the lowest. On the one hand, the CdS QDs, $CdIn_2S_4$, and $CdWO_4$ have well-matched energy band structures and can improve the separation efficiency of photo-generated electrons-holes. On the other hand, CdS QDs with high electron transfer ability can act as an intermediate medium for electron transfer, reducing the recombination of photoelectron-holes. The combination of the both sides promotes the best photocatalytic performance of CdS QDs@$CdIn_2S_4$/$CdWO_4$.

N_2 adsorption-desorption isotherms

In order to investigate the surface physicochemical properties of $CdWO_4$, CdS QDs@$CdWO_4$, CdS QDs@$CdIn_2S_4$/$CdWO_4$, and CdS/$CdWO_4$ (x = 2), N_2 adsorption-desorption tests were performed. The results are shown in Fig. 7. As can be seen from Fig. 7a, b, the N_2 adsorption-desorption isotherm types for both $CdWO_4$ and CdS/$CdWO_4$ (x = 2) are type III with H3 type hysteresis loops. This type of adsorption is due to

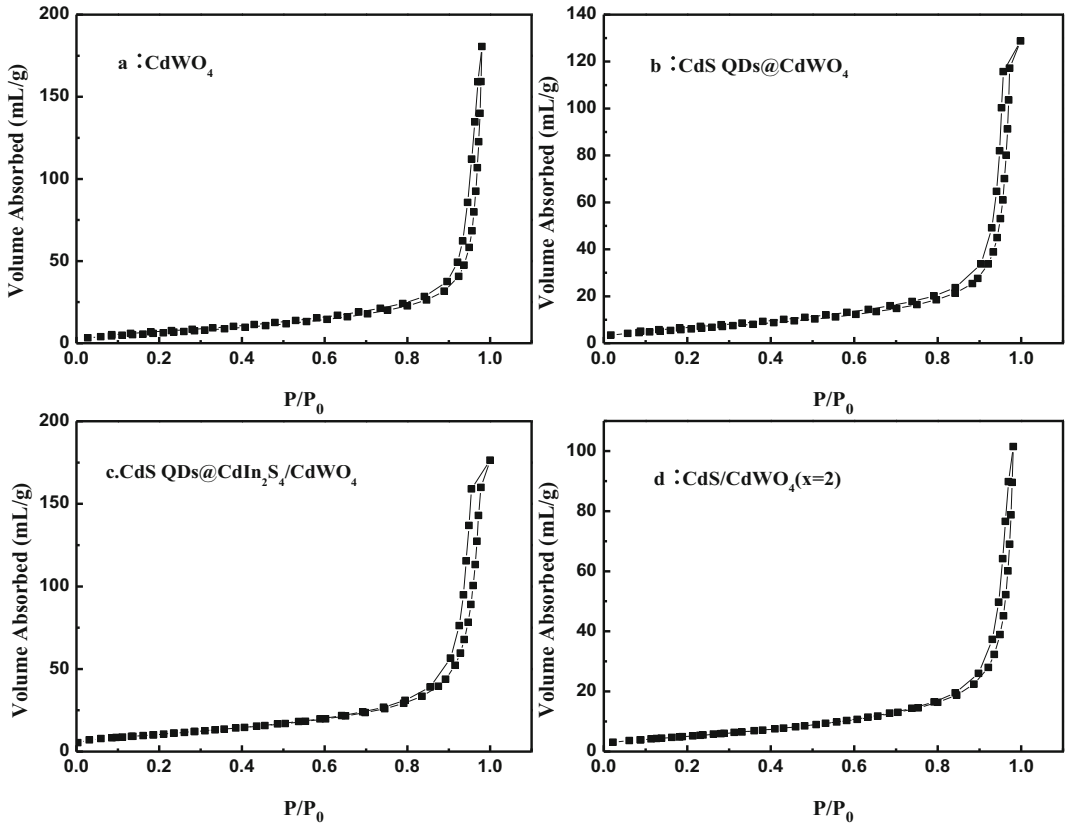

Fig. 7 Nitrogen adsorption-desorption isotherms of $CdWO_4$ (**a**), CdS QDs@$CdWO_4$ (**b**), CdS QDs@$CdIn_2S_4$/$CdWO_4$ (**c**), and CdS/$CdWO_4$(x = 2) (**d**)

the interaction of adsorption of the adsorbate, and the H3 type hysteresis loop reflects the flake-like structure of the material, which is consistent with the morphology of the catalyst observed in the TEM. While observed in Fig. S5a, d, the sample has two distributions of average pore size, which can be attributed to the pores of the material itself and the slit pores caused by the flaky grain structure, respectively.

The N_2 adsorption-desorption isotherms of both CdS QDs@$CdWO_4$ and CdS QDs@$CdIn_2S_4$/$CdWO_4$ in Fig. 7b, c are type V with H2 hysteresis loop, which is due to porous adsorption and the capillary condensation phenomenon, and the H2 type hysteresis loop shows that the pore structure of the material is complex and unevenly distributed, which is consistent with the situation of Fig. S5b, c. The BET specific surface area, pore volume, and average pore size of each material are shown in Table 3. The specific surface area of CdS QDs@$CdWO_4$ is larger than that of CdS/$CdWO_4$ (x = 2). This is mainly due to the fact that the small particles of CdS QDs are loaded on $CdWO_4$. However, the specific surface area of the CdS QDs@$CdIn_2S_4$/$CdWO_4$ sample is the largest, which can be attributed to the fact that the structure of the catalyst surface is changed by two microwave radiation when the catalyst is synthesized. It also makes CdS QDs@$CdIn_2S_4$/$CdWO_4$ exhibits an optimal activity under multi-mode photocatalysis.

Photocatalytic performance

In order to investigate the photocatalytic properties of the synthesized products, the composite photocatalysts CdS/$CdWO_4$ (x = 2, 3, 4) were used for photocatalytic degradation of MO under UV, visible light and simulated sunlight. As can be seen from Fig. 8a, different catalysts have better degradation effect on the MO solution under the irradiation of ultraviolet light, wherein the activity of the composite material is better than the commercial P25, $CdWO_4$, and CdS. The order of catalytic activity in CdS/$CdWO_4$ (x = 2, 3, 4) series materials is CdS/$CdWO_4$ (x = 2) > CdS/$CdWO_4$ (x = 3) > CdS/$CdWO_4$ (x = 4). This result is due to the formation of nano-heterojunctions CdS/$CdWO_4$ (x = 2, 3, 4) after $CdWO_4$ and CdS compounding, which increases the separation of electron-hole pairs, prolongs the lifetime of photogenerated carriers, and improves the catalyst degradation efficiency. Among them, the activity of the sample CdS/$CdWO_4$ (x = 2) is the highest, and this result is mainly consistent with its XRD results. From the XRD, the sample CdS/$CdWO_4$ (x = 2) has a better crystal structure and has a clear characteristic peak of $CdWO_4$ and CdS. Therefore, the ratio of CdS to $CdWO_4$ was synthesized using this optimized condition in the subsequent experiments.

In addition, in order to study the photocatalytic activity of CdS QDs, the experimental scheme was further optimized. First, the CdS QDs precursor solution was synthesized at a fixed charge ratio, and the synthesis time was controlled to prepare a series of CdS QDs@$CdWO_4$ (30, 60, and 90 min) nanocomposites. Figure 8b shows that CdS QDs@$CdWO_4$ (60 min) has the best degradation effect on MO under UV light. It was confirmed that CdS QDs@$CdWO_4$ with a reaction time of 60 min was the best sample. This result can be attributed to the fact that microwave irradiation can promote the precursor solution reaction during the synthesis, which is beneficial to the combination of CdS QDs and $CdWO_4$. If the reaction time is too short, the load of CdS QDs will be low; too high, the load of CdS QDs will be more. This is all not conducive to the improvement of photocatalytic activity. CdS QDs@$CdWO_4$ was significantly better than CdS/$CdWO_4$ (x = 2) for the degradation of MO for 60 min, which was consistent with the PL spectra and N_2 adsorption-desorption analysis results of CdS QDs@$CdWO_4$ and CdS/$CdWO_4$ (x = 2).

Table 3 Average pore diameter (*d*), specific surface area (SBET), and total pore volume (V_{total}) of $CdWO_4$, CdS QDs@$CdWO_4$, CdS/$CdWO_4$ (x = 2), and CdS QDs@$CdIn_2S_4$/$CdWO_4$

Semiconductor	*d*/nm	S_{BET}/(m^2/g)	V_{total}/(cm^3/g)
$CdWO_4$	4.8/34.9	26.0	0.28
CdS QDs@$CdWO_4$	42.1	23.7	0.19
CdS/$CdWO_4$(x = 2)	3.7/41.8	20.1	0.16
CdS QDs@$CdIn_2S_4$/$CdWO_4$	32.7	39.1	0.27

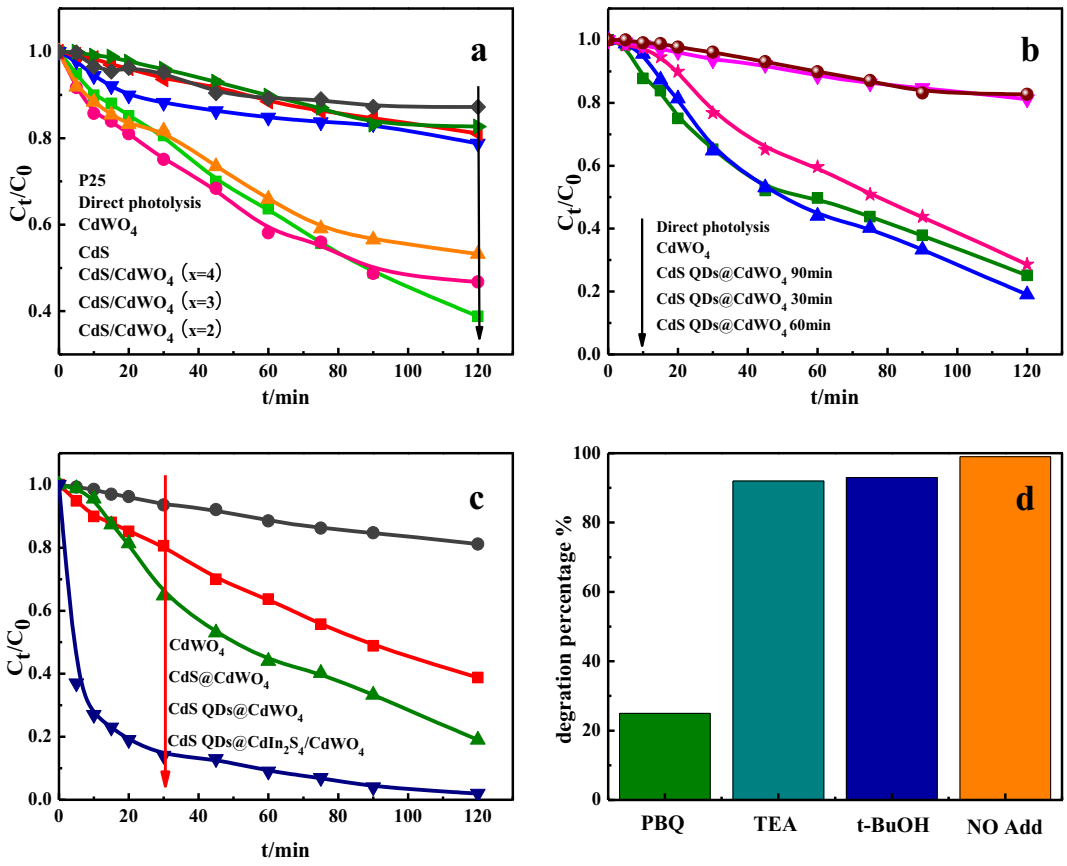

Fig. 8 UV photocatalytic degradation MO profiles result. **a** UV photocatalytic degradation of MO with $CdWO_4$, direct photocatalysis, P25, and different ratio of $CdS/CdWO_4$ catalysts. **b** UV photocatalytic degradation of MO by CdS QDs@$CdWO_4$ with different synthesis time. **c** UV light photocatalytic degradation of MO by monomer, binary, and ternary. **d** Ternary catalyst capture experimental results

Compared with CdS, CdS QDs have high electron transfer efficiency, and the volume of CdS QDs is small. To a certain extent, the specific surface area of CdS QDs@$CdWO_4$ (60 min) is larger than that of $CdS/CdWO_4$ (x = 2), and the presence of CdS QDs will improve the degradation activity of CdS QDs@$CdWO_4$. Figure 8c shows the results of UV degradation of different catalysts. It can be seen from Fig. 8c that CdS QDs@$CdIn_2S_4/CdWO_4$ shows an excellent photocatalytic activity for the degradation of MO. MO solution is almost colorless after photocatalytic reaction carries out 60 min.

Figure 9a shows the experimental results of visible light catalytic degradation of MO on different catalysts. Under visible light irradiation, CdS QDs@$CdIn_2S_4/CdWO_4$ still showed good photocatalytic activity for degrading MO. In order to study the kinetic characteristics of the reaction, the kinetics results of different catalysts are plotted in Fig. 9b. The kinetic formula is that:

$$-\ln C_t/C_0 = kt$$

Among them, C_t is the concentration value (mg/L) of the dye at time t, C_0 is the concentration value (mg/L) when the dye is started, and k is the rate constant (min^{-1}). From Fig. 9b, it can be clearly seen that $-\ln C_t/C_0$ of the direct solution, P25, $CdWO_4$, CdS, CdS QDs@$CdWO_4$, $CdS/CdWO_4$, and CdS QDs@$CdIn_2S_4/CdWO_4$ is basically linear with the reaction time t, indicating that different catalyst degradation of the dye MO follows pseudo-first-order reaction kinetics. And the rate constants of each catalytic reaction under different conditions are 3.26×10^{-5}, 3.14×10^{-5}, 7.89×10^{-5}, 3.01×10^{-5}, 2.33×10^{-4}, 2.88×10^{-4}, and 5.30×10^{-4} min^{-1}. It is worth noting that CdS QDs@$CdIn_2S_4/CdWO_4$ also

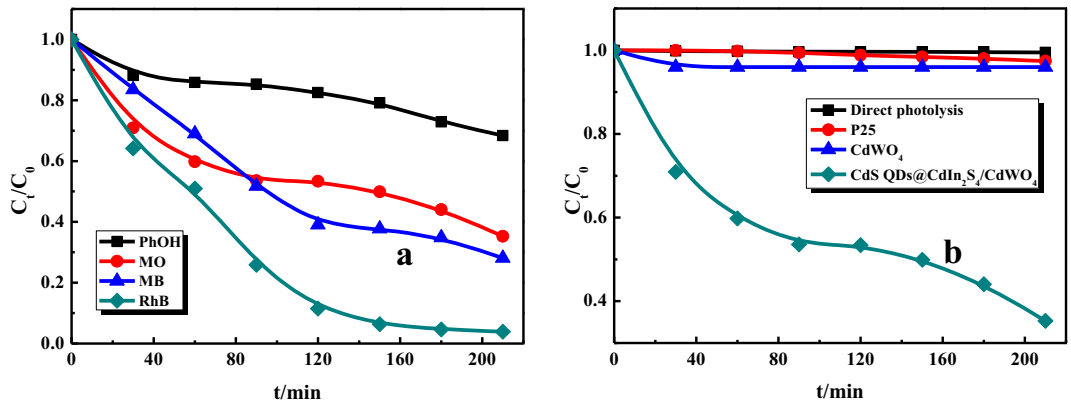

Fig. 10 Simulated sunlight photocatalytic degradation MO profiles result. **a** CdS QDs@$CdIn_2S_4$/$CdWO_4$ under simulated sunlight photocatalytic degradation different dyes. **b** simulated photocatalytic degradation of MO under simulated sunlight

exhibits good activity in the degradation of MO under simulated sunlight (see Fig. 10b) and also has a degradative effect on different dyes (see Fig. 10a). This shows that CdS QDs @$CdIn_2S_4$/$CdWO_4$ nanocomposites have a certain activity for different light sources and different types of dyes.

Why CdS QDs@$CdIn_2S_4$/$CdWO_4$ nanocomposites have excellent degradation effect, according to UV-Vis/DRS, PL, and N_2 adsorption-desorption analysis results, the reason is that the narrow bandgap $CdIn_2S_4$ and CdS QDs are introduced in the synthesis. Both of them combine with $CdWO_4$ can increase the absorption of the composite material in the visible region to a certain extent and can achieve high utilization of sunlight. While matching the energy band structure between semiconductors, weakening the electron and hole and increasing the probability of separation between excited electrons and holes.

In order to investigate the active species of CdS QDs@$CdIn_2S_4$/$CdWO_4$ during the photocatalytic reaction, captured experiments of UV photocatalytic reaction MO were carried out by with p-benzoquinone, triethanolamine, and tertbutyl alcohol as capture agents. In Fig. 8d, when UV irradiation of the MO solution after 75 min, added superoxide radical scavenger (p-benzoquinone) degradation rate was the lowest. The degradation rate did not change much when added the hole trapping agent (triethanolamine) and hydroxyl radical scavenger (tertbutyl alcohol). It can be seen that the main active material in the reaction process of CdS QDs@$CdIn_2S_4$/$CdWO_4$ nanocomposites is the superoxide radical.

In addition, in order to study the photocatalytic hydrogen production performance of CdS QDs@$CdIn_2S_4$/$CdWO_4$ nanocomposites in this paper, photocatalytic hydrogen production activity of CdS QDs@$CdIn_2S_4$/

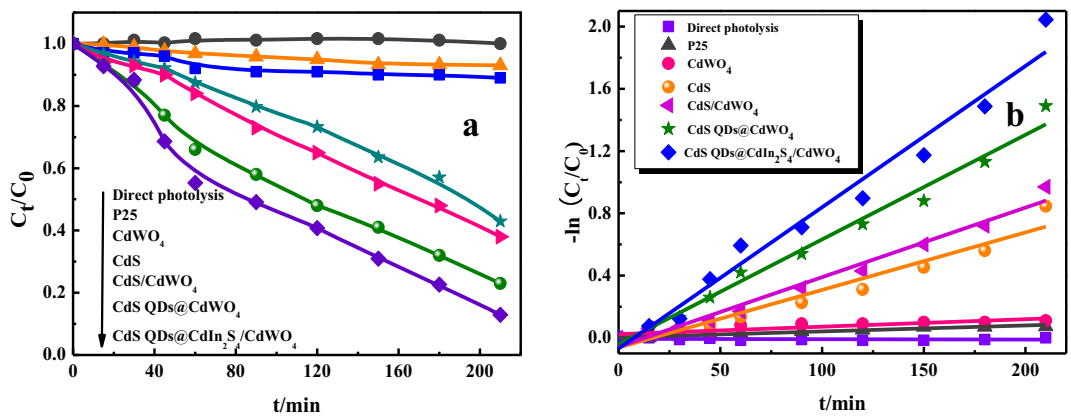

Fig. 9 Visible-light photocatalytic degradation MO profiles result. **a** Graph of degradation of MO by different catalysts. **b** Kinetics of degradation of MO by different catalysts

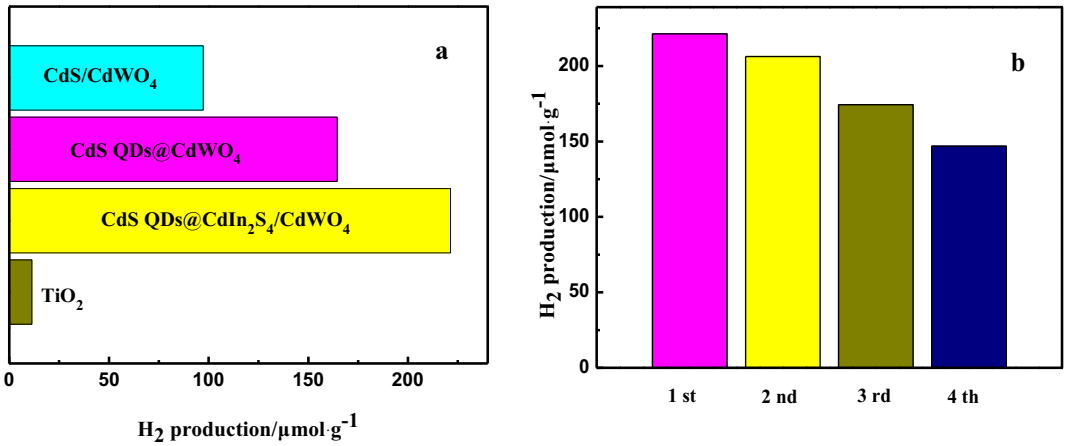

Fig. 11 Comparison of hydrogen production from photolysis of TiO_2, $CdS/CdWO_4$, CdS QDs@$CdWO_4$, and CdS QDs@$CdIn_2S_4/CdWO_4$ (**a**) and results of four cycles of CdS QDs@$CdIn_2S_4/CdWO_4$, hydrogen evolution from hydrogenolysis of water (**b**)

$CdWO_4$ nanocomposites under visible light ($\lambda >$ 420 nm) was investigated. The cut filter was used to remove the UV light from the light source and illuminate the sample for 8 h. The results showed that under the same conditions, the hydrogen evolution amount of the sample CdS QDs@$CdIn_2S_4/CdWO_4$ was 221.3 μmol g^{-1}, while that of the $CdS/CdWO_4$ and CdS QDs@$CdWO_4$ were 97.3 and 164.5 μmol g^{-1}, respectively (Fig. 11a). Obviously, composites modified with CdS QDs have better photolytic hydrogen production capability. The results show that the CdS QDs@$CdWO_4$ hydrogen production is much higher than that of $CdS/CdWO_4$ under visible light. It is further proved that the CdS QDs have high electron transfer efficiency, and thus the photocatalytic water evolution of CdS QDs@$CdWO_4$ is significantly improved.

The above results are further attributed to the fact that during the photocatalytic water splitting process photogenerated electrons on the conduction band of the semiconductor can migrate from the conduction band of $CdIn_2S_4$ to the conduction band of CdS QDs and finally migrate to the conduction band of $CdWO_4$. The well-matched bandgap structure of the three semiconductors is conducive to the electron transfer, and the efficient electron transfer efficiency of the CdS QDs further promotes a large number of transferred electrons on the conduction band of the $CdWO_4$, and thus it is easier to reduce the H_2O to H_2. In order to further examine the photocatalytic recycling capability of CdS QDs@$CdIn_2S_4/CdWO_4$, four cycles of the photocatalyst were tested in Fig. 11b. As can be seen from Fig. 11b, the CdS QDs@$CdIn_2S_4/CdWO_4$ synthesized after four cycles of experiments still has a certain continuous hydrogen production capability.

Possible photocatalytic mechanism of CdS QDs@$CdIn_2S_4/CdWO_4$

The valence band potentials of $CdWO_4$ and CdS QDs were calculated according to the following empirical formulas (1) and (2):

$$E_{CB} = \chi + Ec\text{–}Eg/2 \quad (1)$$

$$E_{VB} = E_{CB} + Eg \quad (2)$$

Among them, Ec is a constant relative to the standard H electrode, $Ec = -4.5Ev$; Eg is the forbidden bandwidth of the semiconductor (based on the actual measurement result); χ is the geometric mean of the absolute electronegativity of each atom in the semiconductor. The enthalpies of $CdWO_4$ and CdS were calculated to be 6.28 and 5.04 eV. The valence band conduction band values of relevant substances in the text are shown in Table 2. Combined with the above capture experiment results, we speculate the possible photocatalytic degradation mechanism of CdS QDs@$CdIn_2S_4/CdWO_4$.

As shown in Fig. 12a–b, CdS QDs@$CdIn_2S_4/CdWO_4$ was excited under the irradiation of light. Light irradiation causes the electrons on $CdIn_2S_4$ to transition from the valence band (VB = − 0.76 eV) to the conduction band (CB = 1.34 eV). Since the conduction band of $CdIn_2S_4$ is more negative than that of CdS QDs (CB = − 0.61 eV), and the conduction band of CdS QDs is also more negative than that of $CdWO_4$ (CB = − 0.07 eV), and thus the electrons on $CdIn_2S_4$ can effectively pass

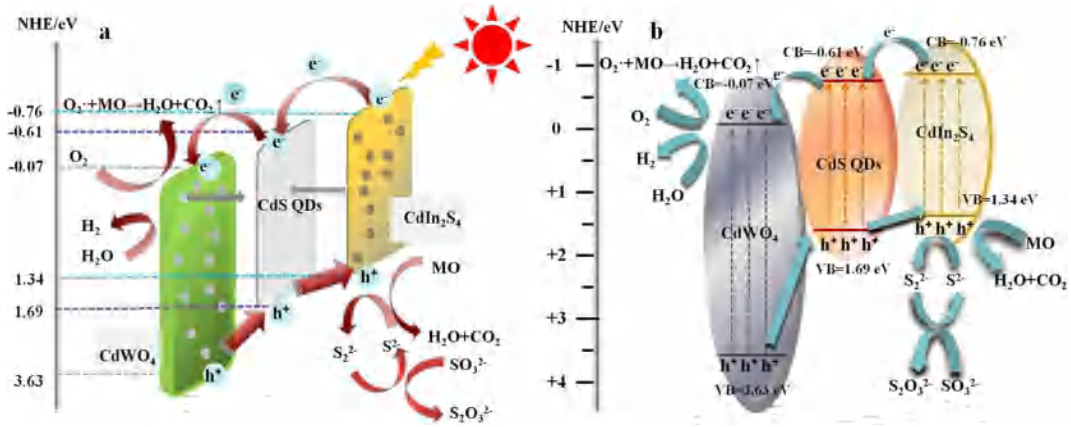

Fig. 12 Possible photocatalytic reaction mechanisms of CdS QDs@$CdIn_2S_4$/$CdWO_4$ (**a**, **b**)

through CdS QDs and eventually transfer to the conduction band of $CdWO_4$. At the same time, the holes on $CdWO_4$ (VB = 3.63 eV) are transferred to the valence band of $CdIn_2S_4$ (VB = 1.34 eV) by CdS QDs (VB = 1.69 eV), so as to realize effective separation of electron-hole pairs. The photogenerated electrons on the $CdWO_4$ conduction band react with O_2 to produce $\cdot O_2^-$. $\cdot O_2^-$, and holes in the valence band of $CdIn_2S_4$ both have highly oxidizing, capable of degrading organic dyes and mineralizing into small molecules of inorganic ions, H_2O and CO_2. $CdIn_2S_4$ ($Eg = 2.1$ eV) and CdS QDs ($Eg = 2.3$ eV) as narrow bandgap semiconductors, the high recombination rate of photogenerated carriers is not conducive to the improvement of photocatalytic activity. The stability of the composite material can be enhanced and light corrosion can be effectively avoided by combination with the wide bandgap semiconductor $CdWO_4$ ($Eg = 3.7$ eV).

At the same time, from the perspective of semiconductor conduction band, photogenerated electrons eventually migrate to the conduction band of $CdWO_4$, which can reduce H_2O to H_2. From the perspective of the valence band of semiconductors, holes in the valence band of $CdIn_2S_4$ will be trapped by S^{2-}, and the resulting S_2^{2-} will compete with the reduction reaction of protons. SO_3^{2-} reacts with S_2^{2-} to generate S^{2-} capable of trapping holes and $S_2O_3^{2-}$ will not compete with photocatalytic reactions. The difference in semiconductor conduction band and valence band potential leads to the migration of photogenerated electrons and holes when the heterojunction of the composite material is formed, which essentially inhibits the recombination of photogenerated electron-hole pairs. In addition, the addition of CdS QDs has become a bridge between photoelectrons and holes transported between $CdIn_2S_4$ and $CdWO_4$. Compared to ordinary CdS, due to the advantages of small QD size, photogenerated electrons and holes migrate more rapidly on CdS QDs and do not recombine in the CdS bulk phase, improving the migration efficiency to a certain extent, thereby improving the photocatalytic activity of the composite material.

Conclusion

In this paper, a kind of CdS QDs modified $CdIn_2S_4$/$CdWO_4$ composites was successfully prepared by microwave-assisted hydrothermal method. CdS QDs modified $CdIn_2S_4$/$CdWO_4$ composites show a suitable specific surface area, a matched band structure between semiconductors and stronger light absorption, which can well degrade organic pollutants under multi-mode conditions. Meanwhile, the hydrogen production of CdS QDs@$CdIn_2S_4$/$CdWO_4$ was 19.6 times higher than that of commercial TiO_2 (P25). On the one hand, its excellent photocatalytic performance is due to the fact that CdS QDs have strong electron transporting ability and can prolong the separation lifetime of photogenerated electron-hole. On the other hand, after the introduction of $CdIn_2S_4$ and CdS QDs, a matching band structure is formed between semiconductors in the composite material CdS QDs@$CdIn_2S_4$/$CdWO_4$, which increases the path of photogenerated electron transfer and can reduce the unnecessary binding of electrons and holes to the surface of the material and further enhance the separation between the excitation electrons and holes. These results bring about an excellent photocatalytic performance of CdS QDs@$CdIn_2S_4$/$CdWO_4$ composite.

Funding information This study is supported by the National Natural Science Foundation of China (21376126, 21776144), the Fundamental Research Funds in Heilongjiang Provincial Universities (135209105), Government of Heilongjiang Province Postdoctoral Grants, China (LBH-Z11108), Postdoctoral Researchers in Heilongjiang Province of China Research Initiation Grant Project (LBH-Q13172), Innovation Project of Qiqihar University Graduate Education (YJSCX2017-021X), College Students' Innovative Entrepreneurial Training Program Funded Projects of Qiqihar University (201810232056), and Qiqihar University in 2016 College Students Academic Innovation Team Funded Projects.

Compliance with ethical standards

Conflict of interest The authors declare that they have no conflict of interest.

References

Aslam I, Cao C, Tanveer M, Farooq MH, Khan WS, Tahir M, Idrees F, Khalid S (2014) A novel Z-scheme WO_3/$CdWO_4$ photocatalyst with enhanced visible-light photocatalytic activity for the degradation of organic pollutants. RSC Adv 5(8):6019–6026. https://doi.org/10.1039/C4RA15847D

Bi Y, Ouyang S, Cao J, Ye J (2011) Facile synthesis of rhombic dodecahedral AgX/Ag_3PO_4 (X = Cl, Br, I) heterocrystals with enhanced photocatalytic properties and stabilities. PCCP 13(21):10071–10075. https://doi.org/10.1039/c1cp20488b

Carević MV, Čomor MI, Mitrić MN, Barudžija TS, Ahrenkiel SP, Abazović ND (2015) The influence of reaction media on $CdIn_2S_4$ and $ZnIn_2S_4$ nanocrystallite formation and growth of mesocrystal structures. CrystEngComm 17:8492–8499. https://doi.org/10.1039/C5CE01432H

Chen X, Li L, Zhang W, Li Y, Song Q, Zhang J, Liu D (2016a) Multi-pathway photoelectron migration in globular flower-like In_2O_3/AgBr/Bi_2WO_6, synthesized by microwave-assisted method with enhanced photocatalytic activity. J Mol Catal A Chem 414(27):27–36. https://doi.org/10.1016/j.molcata.2015.12.023

Chen X, Li L, Zhang W, Li Y, Song Q, Dong L (2016b) Fabricate globular flower-like CuS/$CdIn_2S_4$/$ZnIn_2S_4$ with high visible light response via microwave-assisted one–step method and its multi-pathway photoelectron migration properties for hydrogen evolution and pollutant degradation. ACS Sustanin. Chem Eng 4(12):6680–6688. https://doi.org/10.1021/acssuschemeng.6b01543

Chen W, Huang T, Hua YX, Liu TY, Liu XH, Chen S (2016c) Hierarchical $CdIn_2S_4$ microspheres wrapped by mesoporous g-C_3N_4 ultrathin nanosheets with enhanced visible light driven photocatalytic reduction activity. J Hazard Mater 320:529–538. https://doi.org/10.1016/j.jhazmat.2016.08.025

Cheng F, Yin H, Xiang Q (2017) Low-temperature solid-state preparation of ternary CdS/g-C_3N_4/CuS nanocomposites for enhanced visible-light photocatalytic H_2-production activity. Appl Surf Sci 391:432–439. https://doi.org/10.1016/j.apsusc.2016.06.169

Ge L, Zuo F, Liu J, Ma Q, Wang C, Sun D, Bartels L, Feng P (2012) Synthesis and efficient visible light photocatalytic hydrogen evolution of polymeric g-C_3N_4 coupled with CdS quantum dots. J Phys Chem C 116(25):13708–13714. https://doi.org/10.1021/jp3041692

Hussain H, Tocci G, Woolcot T, Torrelles X, Pang CL, Humphrey DS, Yim CM, Grinter DC, Cabailh G, Bikondoa O, Lindsay R, Zegenhagen J, Michaelides A, Thornton G (2017) Structure of a model TiO_2 photocatalytic interface. Nature Mat 16(4):461–4660. https://doi.org/10.1038/nmat4793

Jia X, Tahir M, Pan L, Huang ZF, Zhang X, Wang L, Zou JJ (2016) Direct Z-scheme composite of CdS and oxygen-defected $CdWO_4$: an efficient visible-light-driven photocatalyst for hydrogen evolution. Appl Catal B-Environ 198:154–161. https://doi.org/10.1016/j.apcatb.2016.05.046

Kandi D, Martha S, Parida KM (2017) Quantum dots as enhancer in photocatalytic hydrogen evolution: a review. Int J Hydrog Energy 42(15):9467–9481. https://doi.org/10.1016/j.ijhydene.2017.02.166

Khanchandani S, Srivastava PK, Kumar S, Ghosh S, Ganguli AK (2014) Band gap engineering of ZnO using core/shell morphology with environmentally benign Ag_2S sensitizer for efficient light harvesting and enhanced visible-light photocatalysis. Inorg Chem 53(17):8902–8912. https://doi.org/10.1021/ic500518a

Lei G, Jing L (2011) Efficient visible light-induced photocatalytic degradation of methyl orange by QDs sensitized CdS-Bi_2WO_6. Appl Catal B-Environ 105(3–4):289–297. https://doi.org/10.1016/j.apcatb.2011.04.016

Liu X, Chen Q, Wang R, Wang L, Yu X, Cao J, Zhou Y, Sun H (2015) Simultaneous femtosecond laser doping and surface texturing for implanting applications. Adv Mater Interfaces 2(9). https://doi.org/10.1002/admi.201500058

Ling Y, Zhou L, Tan L, Wang Y, Yu C (2010) Synthesis of urchin-like $CdWO_4$ microspheres via a facile template free hydrothermal method. Crystengcomm 12(10):3019–3026. https://doi.org/10.1039/b927420k

Liang Y, Lin S, Hu J, Li L, McEvoy J G, Cui Wet al (2014) Facile hydrothermal synthesis of nanocomposite Ag@AgCl/$K_2Ti_4O_9$, and photocatalytic degradation under visible light irradiation. J Mol Catal A Chem 383–384(3):231–238. https://doi.org/10.1016/j.molcata.2013.12.014

Ma D, Shi JW, Zou Y, Fan Z, Ji X, Niu C (2017) Highly efficient photocatalyst based on a CdS quantum dots/ZnO Nanosheets 0D/2D heterojunction for hydrogen evolution from water splitting. ACS Appl Mat Interfaces 9(30):25377–25386. https://doi.org/10.1021/acsami.7b08407

Mao P, Qi L, Liu X, Liu Y, Jiao Y, Chen S, Yang Y (2016) Synthesis of Cu/Cu_2O hydrides for enhanced removal of iodide from water. J Hazard Mater 328:21–28. https://doi.org/10.1016/j.jhazmat.2016.12.065

Mahadadalkar MA, Kale SB, Kalubarme RS, Bhirud AP, Ambekar JD, Gosavi SW, Kulkarni MV, Park CJ, Kale BB (2016) Architecture of $CdIn_2S_4$/graphene nano-heterostructure for solar hydrogen production and anode for lithium ion battery. RSC Adv 6(41):34724–34736. https://doi.org/10.1039/C6RA02002J

Mahadadalkar MA, Gosavi SW, Kale BB (2018) Interstitial charge transfer pathways in a TiO_2/$CdIn_2S_4$ heterojunction photocatalyst for direct conversion of sunlight into fuel. J

Mater ChemA 6:16064–16073. https://doi.org/10.1039/c8ta03398f

Mousavikamazani M, Zarghami Z, Salavatiniasari M, Amiri O (2016) $CdIn_2S_4$ quantum dots: novel solvent-free synthesis, characterization and enhancement of dye-sensitized solar cells performance. RSC Adv 6:39801–39809. https://doi.org/10.1039/C6RA03894H

Pan L, Muhammad T, Ma L, Huang ZF, Wang S, Wang L, Zou J, Zhang X (2016) MOF-derived C-doped ZnO prepared via, a two-step calcination for efficient photocatalysis. Appl Catal B-Environ 189:181–191. https://doi.org/10.1016/j.apcatb.2016.02.066

Qian Y, Yang M, Zhang F, Du J, Li K, Lin X, Zhu X, Lu Y, Wang W (2018) A stable and highly efficient visible-light-driven hydrogen evolution porous $CdS/WO_3/TiO_2$, photocatalysts. Mater Charact 142:43–49. https://doi.org/10.1016/j.matchar.2018.05.025

Reddy KG, Deepak TG, Anjusree GS, Thomas S, Vadukumpully S, Subramanian KR, Nair SV, Nair AS (2014) On global energy scenario, dye-sensitized solar cells and the promise of nanotechnology. PCCP 16(15):6838–6858. https://doi.org/10.1039/c3cp55448a

Rokhsat E, Akhavan O (2016) Improving the photocatalytic activity of graphene oxide/ZnO nanorod films by UV irradiation. Appl Surf Sci 371:590–595. https://doi.org/10.1016/j.apsusc.2016.02.222

Shi J, Tong R, Zhou X, Gong Y, Zhang Z, Ji Q, Zhang Y, Fang Q, Gu L, Wang X, Liu Z, Zhang Y (2016) Temperature-mediated selective growth of MoS_2/WS_2 and WS_2/MoS_2 vertical stacks on Au foils for direct photocatalytic. Adv Mater 28(48):10664–10672. https://doi.org/10.1002/adma.201603174

Wang C, Wang L, Jin J, Liu J, Li Y, Wu M, Chen L, Wang B, Yang X, Su B (2016a) Probing effective photocorrosion inhibition and highly improved photocatalytic hydrogen production on monodisperse PANI@CdS core-shell nanospheres. Appl Catal B-Environ 188:351–359. https://doi.org/10.1016/j.apcatb.2016.02.017

Wang CY, Zhang X, Song XN, Wang WK, Yu HQ (2016b) Novel $Bi_{12}O_{15}Cl_6$ photocatalyst for the degradation of bisphenol A under visible-light irradiation. ACS Appl Mat Interfaces 8(8):5320–5326. https://doi.org/10.1021/acsami.5b12092

Wang M, Zhang H, Zu H, Zhang Z, Han J (2018) Construction of TiO_2/CdS heterojunction photocatalysts with enhanced visible light activity. Appl Surf Sci 455:729–735. https://doi.org/10.1016/j.apsusc.2018.06.047

Wang X, Maeda K, Thomas A, Takanabe K, Xin G, Carlsson JM, Domen K, Antonietti M (2009) A metal-free polymeric photocatalyst for hydrogen production from water under visible light. Nat Mater 8(1):76–80. https://doi.org/10.1038/nmat2317

Xia J, Ji M, Di J, Wang B, Yin S, Zhang Q, He M, Li H (2016) Construction of ultrathin $C_3N_4/Bi_4O_5I_2$, layered nanojunctions via ionic liquid with enhanced photocatalytic performance and mechanism insight. Appl Catal B-Environ 191:235–245. https://doi.org/10.1016/j.apcatb.2016.02.058

Xu W, Zheng C, Hua H, Yang Q, Chen L, Xi Y, Hu C (2015) Synthesis and photoelectrochemical properties of $CdWO_4$, and $CdS/CdWO_4$, nanostructures. Appl Surf Sci 327:140–148. https://doi.org/10.1016/j.apsusc.2014.11.156

Yan X, Wu Z, Huang C, Liu K, Shi W (2017) Hydrothermal synthesis of $CdS/CoWO_4$, heterojunctions with enhanced visible light properties toward organic pollutants degradation. Ceram Int 2017 43(7):5388–5395. https://doi.org/10.1016/j.ceramint.2016.12.060

Ye D, Li D, Zhang W, Sun M, Hu Y, Zhang Y, Fu X (2008) A new photocatalyst $CdWO_4$ prepared with a hydrothermal method. J Phys Chem C 112(44):17351–17356. https://doi.org/10.1021/jp8059213

Yu X, Ren N, Qiu J, Sun D, Li L, Liu H (2018) Killing two birds with one stone: to eliminate the toxicity and enhance the photocatalytic property of CdS nanobelts by assembling ultrafine TiO_2 nanowires on them. Sol Energy Mater Sol Cells 183:41–47. https://doi.org/10.1016/j.solmat.2018.04.003

Zang H, Li H, Makarov NS, Velizhanin KA, Wu K, Park YS, Klimov VI (2017) Thick-shell $CuInS_2$/ZnS quantum dots with suppressed "blinking" and narrow single-particle emission line widths. Nano Lett 17(3):1787–1795. https://doi.org/10.1021/acs.nanolett.6b05118

Zhan F, Li J, Li W, Yang Y, Liu W, Li Y (2016) In situ synthesis of $CdS/CdWO_4/WO_3$, heterojunction films with enhanced photoelectrochemical properties. J Power Sources 325(20):591–597. https://doi.org/10.1016/j.jpowsour.2016.06.079

Zhang W, Yang H, Fu W, Li M, Li Y, Yu W (2013) Directly hydrothermal growth of $CdIn_2S_4$, nanosheet films on FTO substrates for photoelectric application. J Alloy Compd 561(10):10–15. https://doi.org/10.1016/j.jallcom.2013.01.196

Zhang C, Guo D, Xu W, Hu C, Chen Y (2016) Radiative/nonradiative recombination affected by defects and electron-phone coupling in $CdWO_4$ nanorods. J Phys Chem C 120(22):12218–12225. https://doi.org/10.1021/acs.jpcc.6b04145

Zheng Y, Hirayama M, Taminato S, Lee S, Oshima Y, Takayanagi K, Suzuki K, Kanno R (2015) Reversible lithium intercalation in a lithium-rich layered rocksalt Li_2RuO_3, cathode through a Li_3PO_4, solid electrolyte. J Power Sources 300:413–418. https://doi.org/10.1016/j.jpowsour.2015.09.097